AIP | Journal of Applied Physics

# Nanopore fabrication in amorphous Si: Viscous flow model and comparison to experiment

H. Bola George, Yuye Tang, Xi Chen, Jiali Li, John W. Hutchinson et al.

Citation: J. Appl. Phys. 108, 014310 (2010); doi: 10.1063/1.3452390
View online: http://dx.doi.org/10.1063/1.3452390
View Table of Contents: http://jap.aip.org/resource/1/JAPIAU/v108/i1
Published by the American Institute of Physics.

# Nanopore fabrication in amorphous Si: Viscous flow model and comparison to experiment

H. Bola George,[1] Yuye Tang,[2] Xi Chen,[2] Jiali Li,[3] John W. Hutchinson,[1] Jene A. Golovchenko,[1,4] and Michael J. Aziz[1]
[1]*Harvard School of Engineering and Applied Sciences, Cambridge, Massachusetts 02138, USA*
[2]*Department of Civil Engineering and Engineering Mechanics, Columbia University, New York, New York 10027, USA*
[3]*Department of Physics, University of Arkansas, Fayetteville, Arkansas 72701, USA*
[4]*Department of Physics, Harvard University, Cambridge, Massachusetts 02138, USA*

(Received 22 January 2010; accepted 19 May 2010; published online 7 July 2010)

Nanopores fabricated in free-standing amorphous silicon thin films were observed to close under 3 keV argon ion irradiation. The closing rate, measured *in situ*, exhibited a memory effect: at the same instantaneous radius, pores that started larger close more slowly. An ion-stimulated viscous flow model is developed and solved in both a simple analytical approximation for the small-deformation limit and in a finite element solution for large deformations. The finite-element solution exhibits surprising changes in cross-section morphology, which may be extremely valuable for single biomolecule detection, and are untested experimentally. The finite-element solution reproduces the shape of the measured nanopore radius versus fluence behavior and the sign and magnitude of the measured memory effect. We discuss aspects of the experimental data not reproduced by the model, and successes and failures of the competing adatom diffusion model. © *2010 American Institute of Physics*. [doi:10.1063/1.3452390]

## I. INTRODUCTION

Ion beams permit the manipulation of solid morphologies with single-digit nanometer topography control.[1] Consequently, the fabrication of a variety of devices requiring morphology control at sublithographic length scales has been envisioned, and devices have been fabricated that interact with biomolecules at molecular dimensions.[1–3]

In ion beam nanosculpting,[1,4,5] a free-standing solid membrane containing a single pore of diameter big enough (~100 nm) to be fabricated by a focused ion beam (FIB) is exposed to an unfocused kilo-electron-volt noble gas ion beam and is observed to close; a cross-sectional image of a closed nanopore in silicon nitride is shown in Fig. 1. With feedback on the ion current transmitted through the nanopore, closure may be interrupted to leave the nanopore with the desired dimensions.

Two mechanisms were identified as potentially responsible for the observed effect. One mechanism is the creation by the ion beam of mobile species (called "adatoms") on the surface, which independently diffuse along the surface until annihilated. One of the annihilation channels is an adatom sink at the edge of the pore, thereby acting to close it. The adatom diffusion model developed to explain this effect accounts well for the time-dependence of the pore area and the observed effects of ion beam flux, flux pulsing, and substrate temperature on the sculpting of nanopores in amorphous silicon nitride and silicon dioxide.[1,6]

Another mechanism, identified but not elaborated upon in the original report,[1] is the creation by the ion beam of a very thin, stressed viscous surface layer, where compressive stress caused by the ion beam is relieved; viscous flow of the thin surface layer with a viscosity reduced by ion irradiation acts to close the pore.

In this paper, we present a quantitative ion-stimulated viscous flow model to elaborate the latter mechanism. We also report experiments on the closure of nanopores in amorphous silicon (a-Si), a well-studied material in which we expect to minimize the unknown effects of uncontrolled surface composition changes that might arise from differential sputtering in a compound such as silicon nitride or silicon dioxide. Finally we compare the model to the experimental results and discuss the relative advantages of the ion-stimulated viscous flow model and the adatom diffusion model.

## II. EXPERIMENT

Free-standing silicon nitride ($SiN_x$) membranes of dimensions $30\times30$ $\mu m^2$ supported along their perimeters

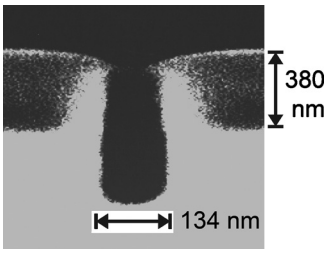


FIG. 1. Image of argon ion beam closed nanopore taken in secondary electron detection imaging mode with 50 keV $Ga^+$ primary beam from Micrion 9500 FIB machine after a slot intercepting the initial pore has been milled through a free-standing low-stress silicon nitride membrane to reveal the ion sculpting cross section. Sample is tilted 20.7° from plan view to reveal the cross section. Due to foreshortening, a scale bar of equal apparent length in the horizontal direction measures 134 nm. Material flow from the top surface and filling in of the initial FIB pore immediately adjacent to the surface is clearly seen. Pore was initially drilled with 50 keV $Ga^+$ and subsequently closed completely under 3 keV $Ar^+$ at room temperature at a flux of 1 $Ar^+$ $nm^{-2}$ $s^{-1}$.

 

were created by photolithography and anisotropic wet chemical etching of 250 nm low pressure chemical vapor deposition (LPCVD) $SiN_x/Si(001)$ substrates. The resistivity of the 450 $\mu$m thick, *p*-type Si(001) substrates is 1–20 $\Omega$ cm. To reduce potential Ga contamination, we first milled the pores in the free-standing $SiN_x$ membranes prior to depositing the amorphous silicon (*a*-Si) film. We used a 50 keV gallium ion ($Ga^{2+}$) FIB FEI/Micrion 9500 (Peabody, MA) with a 75 $\mu$m aperture at normal incidence to mill pores with different diameters in $SiN_x$ membranes prior to deposition of *a*-Si. The FIB fluence and milling field of view were 5 nC $\mu m^{-2}$ and 10 $\mu$m, respectively. Magnetron sputter deposition of *a*-Si was performed on a substrate nominally at room temperature. The base pressure prior to deposition was $\sim 7.7 \times 10^{-8}$ Torr. The rf power during sputter deposition was 125 W (0.235 A and 530 V). The 99.999% *p*-type Si target with resistivity of 0.005–0.02 $\Omega$ cm was purchased from Lesker. A typical deposition rate was 0.025 nm $s^{-1}$ over the course of a 160 min deposition run resulting in $\sim$250 nm thick films. The argon pressure ($P_{Ar}$) during deposition affects the curvature and stress in the samples. The data reported herein were all obtained from minimally-stressed samples sputter-deposited with $P_{Ar}=10$ mTorr. The *ex situ* measured biaxial tensile stress for these samples was $11 \pm 20$ MPa. Film stresses were determined from measurements of radii of curvature before and after deposition on various Si oxide and nitride substrates; the reported uncertainty is the standard deviation from about ten specimens. Following *a*-Si deposition and prior to ion sculpting, the pore areas were determined using a 60 keV JEOL transmission electron microscopy (TEM).

The details of the ion sculpting chamber are reported elsewhere.[1,4] The chamber features include target neutralization with an electron flood gun and real-time determination of instantaneous pore area via sensitive measurements of the ion current transmitted through the pore. The instantaneous pore radius, *R*, is determined by assuming a circular pore geometry and verified by *ex situ* plan-view TEM observations on pores that were not fully closed. For all sculpting experiments reported here, normal incidence continuous irradiation was performed with 3 keV $Ar^+$ and the ion flux *f* was $0.24 \pm 0.02$ $Ar^+$ $nm^{-2}$ $s^{-1}$. The substrate temperature during ion sculpting was controlled at 80 °C.

The closing curves (*R* versus ion fluence $\phi \equiv ft$) for two *a*-Si pores with initial radii of 160 and 200 nm during sculpting are shown in Fig. 2. From such experiments on a series of *a*-Si nanopores with different initial radii we observe that, during closure, pores retain some "knowledge" of their initial radii: at the same instantaneous radius, pores that started smaller require less argon fluence for further closure, i.e., they close "faster" than pores that started larger. We refer to this as the "memory" effect.

## III. ION STIMULATED VISCOUS FLOW MODEL

For comparison to the experiments we present the results of the phenomenological model that has been shown to describe the evolution of biaxial stress[7–10] and three-dimensional (3D) deformation[11] during mega-electron-volt ion irradiation of $SiO_2$. This phenomenological description has been shown to result from a mechanism of a viscoelastic thermal spike caused by the electronic stopping of the high-energy ion,[12] but other mechanisms may cause the same phenomenological behavior, as discussed later. In the phenomenological model[11] that we will use, 3D deformation is the result of the superposition of several effects according to the following equation for the strain rate $d\varepsilon_{ij}/dt$

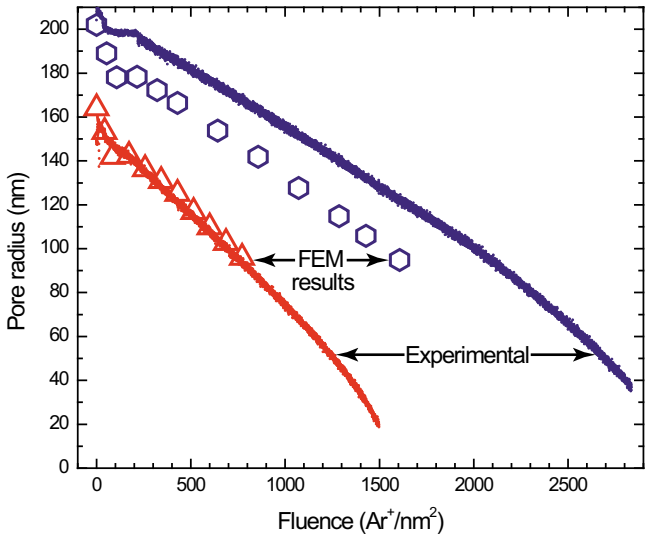


FIG. 2. (Color online) Closure of two *a*-Si nanopores with ion fluence. Experimental initial radii 200 nm and 160 nm; FEM simulation initial radii 202 and 164 nm. The only adjustable parameter in the FEM simulation is *A*, which takes the value $5 \times 10^{-17}$ $cm^2$/ion.

$$\frac{d\varepsilon_{ij}}{dt} = \frac{1}{2\eta} s_{ij} + \frac{1}{2G}\frac{ds_{ij}}{dt} + \delta_{ij}\frac{1}{9B}\frac{d\sigma_{kk}}{dt} + fAD_{ij}. \quad (1)$$

The first three terms on the right-hand side constitute the standard Maxwell model for an isotropic material that shows both elastic and Newtonian-viscous behavior,[13] where $\boldsymbol{\sigma}$ is the stress tensor, $s_{ij}=\sigma_{ij}-\delta_{ij}\sigma_{kk}/3$ the deviatoric stress, $\eta$ the shear viscosity, *B* the bulk modulus, and *G* the shear modulus. In implementing Eq. (1) in the finite element solution in Sec. IV, the time derivative of the stresses is identified with the Jaumann rate and the time derivative of the strains is the Eulerian rate, ensuring that the finite-strain formulation is objective. We assume that irradiation has a negligible effect on the moduli. Ion irradiation is assumed to cause two effects (we have neglected a small additional effect in Otani *et al.* representing a densification effect attributed to a structural transformation in $SiO_2$ but lacking justification in a-Si). The first irradiation-induced effect is an enhanced fluidity, resulting in $\eta$ being flux-dependent and given by

$$\eta = \frac{\eta_{rad}}{f}, \quad (2)$$

where the parameter $\eta_{rad}$ has been shown to depend on temperature and nuclear stopping cross section.[8,9] The second irradiation-induced effect is the superposition of anisotropic strain radially outward from the ion track according to the last term on the right-hand side. *A* is the lone fitting parameter in the model and **D** is a dimensionless anisotropic tensor with cylindrical symmetry about the ion track as described

by Otani *et al.*[11] $A$ is observed to be dependent on sample temperature and ion beam energy and appears to scale with the electronic stopping of the beam.[10] This effect is well established for mega-electron-volt ion energies,[9,11,12] for which electronic stopping dominates over nuclear stopping; however, for 3 keV $Ar^+$ on Si, electronic stopping is only ~10% of the total nuclear+electronic stopping. Nevertheless, this effect appears to quantitatively describe ion beam induced deflections for 50 keV $Ga^+$ in $SiN_x$,[14] where electronic stopping is only ~10% of the total stopping. In this latter case, a phenomenological model based on this anisotropic deformation term provided surprisingly good quantitative agreement with the measured deflection profiles of both low-stress and high-stress silicon nitride free-standing membranes supported at their edges. In that case, as in the case we study in the current paper, and in contrast to the case of mega-electron-volt irradiation where electronic stopping dominates, the final term of Eq. (1) is advanced as a phenomenological working hypothesis, to be tested by comparison to experiment rather than by derivation from a fundamental mechanism.

### A. Insights from dimensional analysis

The complete list of physical parameters and their dimensions as they appear in the models developed in this paper are: time, $t$(s); the initial radius of the pore, $R_0$(m); the thickness of the irradiated layer, $h$(m); the Young's modulus and Poisson's ratio of the Si, $E$(Pa), and $\nu$; the lateral spreading rate of an unconstrained irradiated layer, $fA(s^{-1})$; and the viscosity of the material in the irradiated layer, $\eta$(Pa s). Four dimensionless parameters govern the model solutions: $fAt$, $h/R_0$, $fA\eta/E$, and $\nu$. The stresses are driven by the radiation and are of magnitude $fA\eta$. Consequently, the elastic strains are of magnitude $fA\eta/E$ which, for the present system, is $A\eta_{\mathrm{rad}}/E=(5\times10^{-17}\ \mathrm{cm^2/Ar^+})(1\times10^{24}\ \mathrm{Pa\ Ar^+/cm^2})/(125\ \mathrm{GPa})=4\times10^{-4}$. It follows that the elastic strains are so small compared to the strains of order unity due to viscous deformation that they play a negligible role with regard to the shape evolution. Hence the value of $\nu$ also has negligible effect on the shape evolution. While elasticity will be included in the numerical modeling in Sec. III B, its influence is very small and will be neglected outright in the simple analytical model presented here. The implication of $fA\eta/E$ being very small is that, while the stresses—which are directly measurable—scale with this parameter, the evolving shape of the void is affected negligibly by the elasticity and the viscosity. The dimensional analysis given below makes use of this argument.

Because the last two of the four dimensionless parameters are unimportant for determining the morphology evolution, dimensional analysis implies that if $R(t)$ and $V(t)$ are the pore inner radius and its inward velocity at time $t$,

$$R(t) = R_0 g_R(fAt, h/R_0) \tag{3}$$

and

$$V(t) = hfA g_V(fAt, h/R_0), \tag{4}$$

where $g_R$ and $g_V$ are dimensionless functions.

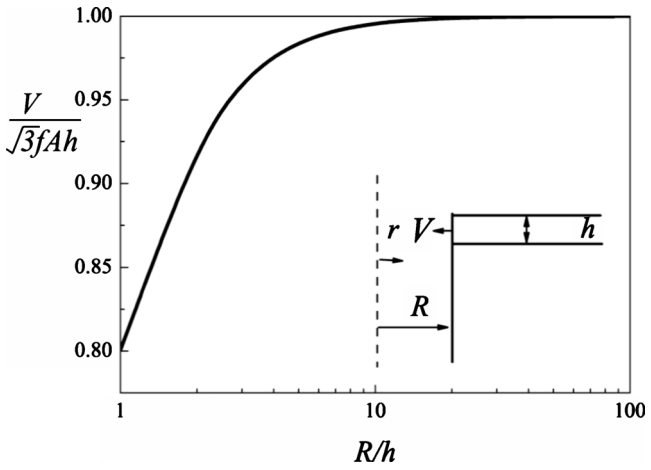


FIG. 3. Inward flow velocity at pore edge vs ratio of instantaneous pore radius to layer thickness from simple model.

### B. Simple analytical model

The analytical model (see inset in Fig. 3) is for an irradiated layer of uniform thickness $h$ and fully supported by a substrate for $r \geq R$. The finite element solution discussed in Sec. IV shows that as the layer spreads inward it generates its own underlying stationary substrate. Only a relatively small annular portion of the layer near the inner edge has thickness less than $h$ such that it has no constraint from below. This unsupported portion of the layer is neglected in the analytical model, which assume a layer of thickness $h$ (the presumed depth of both ion irradiation effects) on a rigid substrate. The inward velocity $V$ at the inner radius $R$ will be determined and then integrated to obtain the evolution of $R$. The model is axisymmetric with in-plane stresses, $\sigma_{rr}$ and $\sigma_{\theta\theta}$, that are averaged through the layer, as are the in-plane strain rates, $\dot{\varepsilon}_{rr}$ and $\dot{\varepsilon}_{\theta\theta}$. The radial shear stress acting on the layer by the underlying substrate is denoted by $\tau$. The radial equilibrium equation for the layer is

$$\frac{1}{r}\frac{d(r\sigma_{rr})}{dr} - \frac{1}{r}\sigma_{\theta\theta} - \tau\frac{1}{h} = 0. \tag{5}$$

With elastic strain rates neglected, the strain-rates from Eq. (1) are

$$\dot{\varepsilon}_{rr} = \frac{1}{2\eta}s_{rr} + fA, \quad \dot{\varepsilon}_{\theta\theta} = \frac{1}{2\eta}s_{\theta\theta} + fA, \tag{6}$$

where, assuming $\sigma_{zz}=0$, the deviator stress components are $s_{rr}=(2\sigma_{rr}-\sigma_{\theta\theta})/3$ and $s_{\theta\theta}=(2\sigma_{\theta\theta}-\sigma_{rr})/3$. We make the following ansatz about the distribution of the radial velocity through the thickness of the layer: $v_r(r,z)=3\bar{v}(r)[z/h-(z/h)^2/2]$, where $\bar{v}(r)$ is the average and $z$ is the out-of-plane coordinate. Consequently the shear rate, $\dot{\varepsilon}_{rz} \cong (1/2)\partial v_r/\partial z$, vanishes at the free surface and is equal to $3\bar{v}/h$ at the interface with the substrate such that $\tau=3\eta\bar{v}/h$. The in-plane strain rates are related to the radial velocity by $\dot{\varepsilon}_{rr}=d\bar{v}/dr$ and $\dot{\varepsilon}_{\theta\theta}=\bar{v}/r$. When the stresses in Eq. (5) are expressed in terms of the radial velocity, one finds

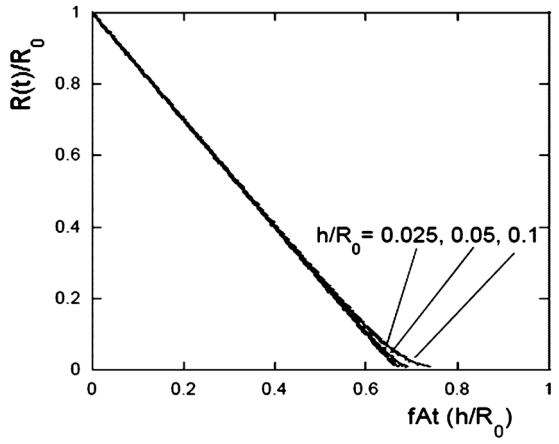


FIG. 4. Normalized closure vs normalized flux in simple model.

$$\frac{d^2\bar{v}}{dr^2} + \frac{1}{r}\frac{d\bar{v}}{dr} - \left(\frac{1}{r^2} + \frac{3}{4h^2}\right)\bar{v} = 0. \tag{7}$$

This equation is supplemented by the requirement that $\bar{v} \to 0$ as $r \to \infty$ and the boundary condition, $\sigma_{rr}=0$ at $r=R$ which requires

$$\frac{d\bar{v}}{dr} + \frac{1}{2r}\bar{v} = \frac{3}{2}fA, \quad r = R. \tag{8}$$

The solution to Eqs. (7) and (8) is

$$\bar{v}(r) = -\sqrt{3}fAh\frac{K_1(\sqrt{3}r/2h)}{K_0(\sqrt{3}R/2h) + (h/\sqrt{3}R)K_1(\sqrt{3}R/2h)} \tag{9}$$

and for $V=-\bar{v}(R)$ is

$$V = \sqrt{3}fAh\frac{K_1(\sqrt{3}R/2h)}{K_0(\sqrt{3}R/2h) + (h/\sqrt{3}R)K_1(\sqrt{3}R/2h)}, \tag{10}$$

where $K_0$ and $K_1$ are modified Bessel functions of the second kind of order zero and one, respectively. The dependence of $V$ on $R/h$ is plotted in Fig. 3, where it is seen that $V$ is essentially $\sqrt{3}fAh$ unless $R/h<10$. The limit $V=\sqrt{3}fAh$ corresponds to the result obtained from a two-dimensional plane strain analysis (with zero strain rate perpendicular to the plane of the insert in Fig. 3).

Equation (10) provides the pore closure velocity at the instantaneous radius $R$. To obtain the time evolution, $R(t)$, integrate Eq. (10) using $V=-dR/dt$ subject to $R=R_0$ at $t=0$ to obtain

$$\int_{R(t)/R_0}^{1} \frac{K_0[(\sqrt{3}R_0/2h)\xi] + \{h/(\sqrt{3}R_0\xi)\}K_1[(\sqrt{3}R_0/2h)\xi]}{K_1[(\sqrt{3}R_0/2h)\xi]}d\xi = \sqrt{3}(fAt)\frac{h}{R_0}. \tag{11}$$

This is an implicit equation for $R(t)/R_0$ in terms of the dimensionless parameters identified in Eqs. (3) and (4). Because we are integrating with respect to the instantaneous radius at each stage, Eq. (11) is valid for finite change in radius. Curves of $R(t)/R_0$ as a function of $fAt(h/R_0)$ are shown for various $h/R_0$ in Fig. 4. The exceptionally weak dependence on $h/R_0$ in this dimensionless plot stems from the fact that $V \cong \sqrt{3}fAh$ except when $R/h<10$. If one integrates $dR/dt=-\sqrt{3}fAh$ subject to $R=R_0$ at $t=0$, one obtains

$$\frac{R(t)}{R_0} = 1 - \sqrt{3}fAt\frac{h}{R_0}. \tag{12}$$

This limit gives an accurate description of the behavior of the model, except for the final stages of closure when the condition $R/h<10$ breaks down.

Among the limitations of the analytical model are its neglect of the innermost unsupported annular region and its assumption that the layer remains planar, both of which are rectified in the finite element model.

## IV. FINITE ELEMENT MODEL

Numerical solutions of Eq. (1) are obtained by mapping the problem onto an anisotropic thermal expansion problem, as described by Otani *et al.*,[11] and implementing a finite-element approach using ABAQUS (Ref. 15) with finite deformation. An axisymmetric model (shown in Fig. 5) is established for the semi-infinite specimen, and the initial radius of the through hole is taken to be either 164 or 202 nm. The irradiation is assumed to uniformly affect a layer of material from the topmost surface downward (along the ion beam direction), extending to a depth $h$, taken to be 16.4 nm [which is the ion beam projected range of 6.5 nm plus three times[16] the standard deviation of 3.3 nm, estimated from TRIM (Ref. 17)]. The irradiation-affected material is modeled as a "flowing" irradiation-responsive visco-elastic "thin film," rigidly attached across a sharp interface to an elastic "substrate" that experiences no irradiation effect. When the surface topography changes, the interface is assumed to instantaneously track it, i.e., the interface profile is exactly the surface profile translated downward by $h$ in the direction of the ion beam.

The anisotropic flow of the film upon ion irradiation is simulated in the same way as described in previous work.[11] A characteristic relaxation time $\tau_R$ is identified, which depends on $\eta_{\text{rad}}, f$, and the elastic constants. It serves as a second parameter in the model, but it is not treated as a free parameter because we can estimate its value from the published literature, as we show below, and because the morphology evolution is not very sensitive to its value. The relaxation time of the viscoelastic Si film is derived from the Maxwell model as

$$\tau_R = 6\eta_{\text{rad}}\left(\frac{1-v}{Ef}\right). \tag{13}$$

For $a$-Si, we assume Young's modulus and Poisson's ratio are those of c-Si, namely, $E=125$ GPa and $\nu=0.25$, independent of radiation flux. The shielded Si substrate deforms only elastically with same $E$ and $v$ values. We take $f=0.24$ $\text{Ar}^+$ $\text{nm}^{-2}$ $\text{s}^{-1}$, the experimental value. The parameter $\eta_{\text{rad}}$ (units: Pa $\text{cm}^{-2}$) characterizing irradiation-enhanced fluidity is the product of the ion flux and the irradiation induced viscosity $\eta$. Molecular dynamics simulations[18] provide a numerical value for the equivalent of $\eta_{\text{rad}}$ normalized to the number of displacements per atom (dpa) per second $\dot{N}_{\text{DPA}}$ instead of to the incident flux; it is $9.656 \pm 0.012$

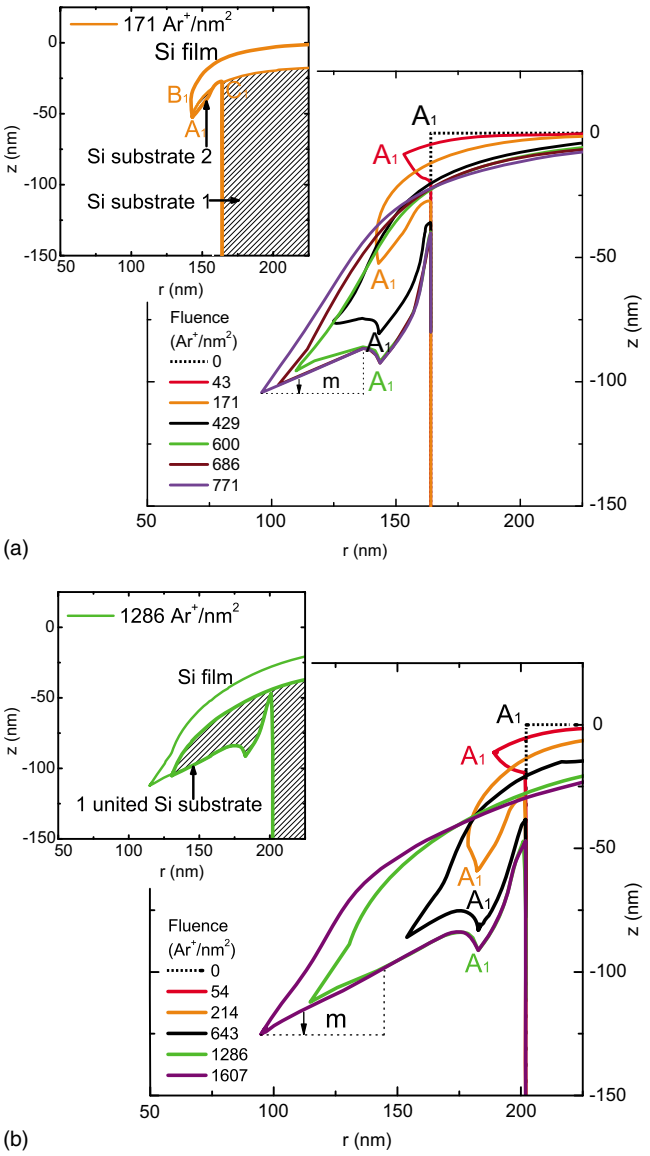


FIG. 5. (Color online) Cross-sectional profiles of the (a) 164 and (b) 202 nm pores from FEM simulation showing mass transport off the pore edges during ion irradiation. Fluences identified correspond to irradiation times in (a) of 0, 179, 713, 1788, 2500, 2858, and 3213 s; (b) 0, 225, 892, 2679, 5358, and 6696 s. Insets: (a) illustration of formation of isolated second elastic substrate underneath viscous layer; (b) illustration of extension of unified single elastic substrate beneath viscous layer.

$\times 10^8$ Pa dpa. We estimated $\dot{N}_{\mathrm{DPA}}$ using the relations

$$\dot{N}_{\mathrm{DPA}} = \left(\frac{\Omega f}{d}\right) N_{\mathrm{recoils}} \tag{14}$$

and

$$N_{\mathrm{recoils}} = 0.8\frac{E}{2E_D}, \tag{15}$$

where $\Omega = 0.02$ nm$^3$ is the volume per Si atom; $d$ is the thickness in which displacements occur (assumed equal to $h$, 16.4 nm); $N_{\mathrm{recoils}}$ is the number of displacements generated per incident ion obtained using Eq. (15), the empirically-determined Kinchin–Pease relation;[19,20] and the displacement energy $E_D$ of Si equals 15 eV.[21] Thus, for 3 keV Ar$^+$ irradiation of Si at the experimental flux, we obtain $\dot{N}_{\mathrm{DPA}} = 2.34 \times 10^{-2}$ dpa per second resulting in $\eta = 4.12 \times 10^{10}$ Pa s, or $\eta_{\mathrm{rad}} = 9.9 \times 10^{23}$ Pa ion/cm$^2$. Hence $\tau_R \approx 1.48$ s.

A constant ion flux is "switched on" at the beginning of the simulation, which allows the time-dependent shear stress to approach a quasistationary value. To update the geometry, the simulation was divided into multiple substeps. In each substep, the profiles (and relevant properties) of the Si film and the substrate are updated based on the current surface morphology, and the residual stress is inherited from the last substep. The cross-sectional profile of the substrate was tracked every substep until a quasistationary profile with a nearly steady closing rate was reached.

The evolution of cross-sectional profile of the material upon continuous ion irradiation is shown in Fig. 5. Because the top surface of the "flowing" Si film is traction-free whereas its bottom is constrained, the extruded tip of the film experiences rotation. The rotation pivot (point $C_1$ of inset) is located at the interface at the inner wall of the Si pore (which continuously changes as the morphology evolves). For the 164 nm Si pore, point $A_1$, representing the initial minimum pore size, moves both inward and downward until $\phi = 171$ Ar$^+$ nm$^{-2}$ (or until $\phi = 214$ Ar$^+$ nm$^{-2}$ for the 202 nm pore). At this moment, point $A_1$ and its surrounding material become too deep to be reached by the irradiation, and flow is suspended in local regions. This results in the formation of an isolated small piece of "substrate," as shown in the inset of Fig. 5(a). Point $B_1$ on the top surface starts to move forward [inset of Fig. 5(a)] and emerges later as a new tip.

With further increase in the irradiation time, the part of the material under irradiation continues to move inward and rotate about its instantaneous pivot, and the new tip becomes more pronounced. At $\phi = 600$ Ar$^+$ nm$^{-2}$ for the 164 nm Si pore (1286 Ar$^+$ nm$^{-2}$ for the 202 nm pore), the isolated pieces of Si "substrate" coalesce to form a continuous substrate [see inset of Fig. 5(b)]. Thereafter, the position of point $A_1$ is fixed, the volume of the extruded Si tip increases as a result of material flow, the tip approaches a quasistationary shape, and the closing rate approaches a quasistationary value. The resulting pore radius versus fluence behavior, shown by the open symbols in Fig. 2, agrees reasonably well with experimental results. After the decay of the initial transient behavior, the simulations reproduce the experimental behavior in both the general shape of the curves and the sign of the "memory effect."

The nanopore closing rate $-dR/d\phi$ is plotted as a function of the instantaneous pore radius $R$ in Fig. 6. In the simulations for small (165 nm) and large (202 nm) initial pore radii, in an initial transient the evolution trend changes rapidly at $R = 140$ nm and 180 nm, respectively, as a result of forming the second isolated Si "substrate" in simulation. The steady state closing rate is established at around $R = 110$ nm and 150 nm, respectively. At steady-state, the slope $m$ of the bottom surface of the extruded region approaches a constant, $m \approx 0.4$ and 0.5, respectively (Fig. 5). The larger value of $m$ is obtained for the larger Si pore. This may happen because in the simple analytical model the slope of the trajectory of the leading edge of the "flowing" Si is steeper for larger pores, as shown in the Appendix, but a

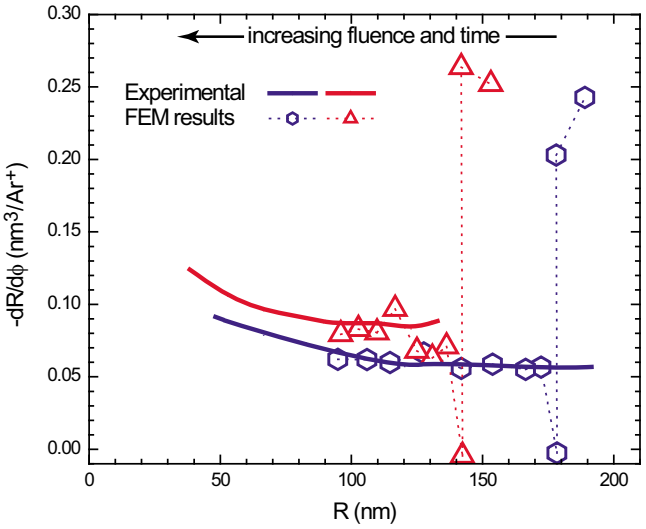


FIG. 6. (Color online) Nanopore closing rates $-dR/d\phi$ vs instantaneous pore radius $R$ for $a$-Si pores under 0.24 $Ar^+$ $nm^{-2}$ $s^{-1}$. Experimental data are smoothed.

rigorous causal relationship between leading edge trajectory and quasistationary slope of the bottom surface has not been established.

## V. DISCUSSION

Both the viscous pore closing finite-element model and the adatom diffusion model[1] reproduce the shape of the pore radius versus fluence curve (Fig. 2) reasonably well. Additionally, the viscous pore closing model reproduces the "memory effect" of Figs. 2 and 6. In the adatom diffusion model, the quasistationary closing rate is independent of the prior history of the pore radius and so does not explain the memory effect.

We observe a qualitatively similar memory effect in silicon dioxide pores with different initial areas irradiated under nominally identical conditions at room temperature. In $SiO_2$, large accretions of matter ~100 nm from the pore resembling volcanoes have been observed, and have been identified with the influence of large electrostatic fields.[22] Such fields are likely to be much smaller in semiconductors and conductors, and on the a-Si pores we have found small topographic features[23] in atomic force microscopy—much smaller than the $SiO_2$ volcanoes. Their influence on the memory effect is unknown.

Although the potential for uncontrolled chemical composition effects is not entirely eliminated due to the potential incorporation of argon into the viscous amorphous layer, the total influence of composition effects on nanopore closure in amorphous silicon is expected to be smaller than that in silicon nitride and silicon dioxide due to the potential for differential sputter yield induced disproportionation in the compounds.

The viscous pore closing model in its current form displays no effect of flux on the relationship between $R$ and fluence and so cannot account for this aspect of the data of Li *et al.*[1] for silicon nitride. The adatom diffusion model explains the flux effect readily: higher fluxes increase the probability that a given adatom is annihilated by ion impingement instead of sinking at the pore edge, thereby reducing the amount of pore closing per unit fluence. In order for the viscous pore closing model to exhibit a flux effect, the flux-dependence of the ion-stimulated viscosity would need to have a functional form other than the reciprocal relationship of Eq. (2). It is not clear whether the viscous pore closing model can explain the flux pulsing effect of Li *et al.*, wherein pulsing the flux increases the amount of closure per unit fluence. In the case of ion-stimulated anisotropic expansion and enhanced fluidity, it is reasonable to suppose that turning the beam off will lead to some morphological evolution toward pore closure as the viscous film relaxes into the pore in order to relieve stress. It is also reasonable to suppose that point defects responsible for fluidity do not disappear instantly upon cessation of irradiation but rather take some time to annihilate or deactivate. The interplay of the ending transient defect concentration, stress, and topography change could create a net effect of flux pulsing, but extending the model along these lines would require introducing several free parameters.

At low temperatures in a-Si and silicon nitride, pores open under the same ion beam that acts to close them at higher temperature.[1,23] This can be rationalized within the adatom diffusion model as the "freezing out" of thermally activated adatom diffusion. The origin of such a trend within the context of the viscous layer model would have to be a temperature-induced change in the sign of the anisotropic deformation parameter $A$. The temperature dependence is unknown for a-Si, but in a-$SiO_2$ $A$ goes from positive to negative with increasing temperature[9]—this would cause the opposite effect, as can be seen from Eq. (12). We have observed[23] that $SiO_2$ pores do not open at temperatures as low as room temperature, and that the closing rate is imperceptibly temperature-dependent over the range 28–64 °C, whereas pores in a-Si close above 50 °C and open below that temperature. A direct comparison of the behavior in $SiO_2$ with the measured temperature-dependence of $A$ is not possible because of the different electronic stopping conditions in the two experiments.

The fitted value of $A$ is $5\times10^{-17}$ $cm^2/ion$ for a-Si under 3 keV $Ar^+$ irradiation at 80 °C. This is twice the value found[24] for a-Si irradiated at 77 K by 30 MeV $Cu^+$, for which the electronic stopping is almost two orders of magnitude greater. Although the possibility of a strong temperature effect, as in a-$SiO_2$, precludes a direct comparison, it is quite possible that the effect we are observing is due to a mechanism other than the electronic stopping mechanism modeled by van Dillen *et al.*,[12] such as isotropic dilatation from implantation plus sputter erosion from the topmost surface. These mechanisms may be indistinguishable in the small-rotation limit of the simple analytical model, but would be distinguishable in the details of the evolving shape calculated from finite element method (FEM), because in the alternative mechanism, the axis of anisotropy would follow the surface normal rather than the ion beam. Experimentally we don't yet have the resolution to resolve the cross-section shapes, so our experimental measurements of pore area versus fluence may not be able to distinguish between these mechanisms.

The viscous layer model (both analytical and finite-element) neglects sputter erosion, which acts around the pore's perimeter to open it and must be more than counteracted by the anisotropic deformation effect in order to yield pore closure. Thus the fitted value of the anisotropic deformation parameter $A$ may be considered a lower limit. Sputter erosion might be responsible for a significant shape change—either blunting or sharpening[25] of the edge of the pore in cross section.

The micrograph in Fig. 1 qualitatively confirms several cross-sectional geometry predictions of the finite-element viscous flow model. These include a convex shape to the ion beam exposed surface near the pore, and significant mass transport into the pore in a thin layer near this surface. Due to FIB sectioning and imaging induced damage and to the instrument's inherent resolution, the image cannot confirm the presence or absence of the very sharp features predicted in Fig. 5. The adatom diffusion model does not make predictions about the cross-sectional morphology.

The viscous layer model (both analytical and finite-element) neglects effects of capillary forces. These stresses are negligible for sufficiently large radii of curvature, but cannot be neglected when the curvatures become as tight as those at the pore radius in the high-fluence profiles shown in Fig. 5. Order-of-magnitude estimates of the relevant radius of curvature below which capillary effects should be important come from comparing capillary-induced effects with the effects contributing to deformation in the model. Comparing the capillary-induced strain rate $\gamma/(\rho\eta)$, where $\gamma$ is the surface free energy and $\rho$ is the local radius of curvature, with the anisotropic deformation rate $fA$ results in an order-of-magnitude value of $\rho=\gamma/(fA\eta)=\gamma/(A\eta_{\mathrm{rad}})$ for the local radius of curvature below which capillary effects should become important. With the surface free energy assumed to be that of unirradiated c-Si, roughly 1 $\mathrm{J/m^2}$,[26] we find $\rho \approx 20$ nm. If instead we compare the capillary-induced stress $\gamma/\rho$ with ion-induced shear stress $\tau$, which is roughly of magnitude $\tau \approx G\tau_R\dot{\gamma} \approx G\tau_R fA$, we have $\rho=\gamma/(G\tau_R fA)$. With $G=E/[2(1+\nu)]=50$ GPa, ion-induced shear stresses are roughly of magnitude 0.08 GPa. The capillary stress is of the same magnitude when the local radius of curvature is roughly 10 nm. Because near the pore radius, where the local radius of curvature is tightest, the extruded material is unsupported by a substrate we expect that there the former tradeoff (capillarity versus anisotropic deformation, $\rho \sim 20$ nm) is more relevant. Hence we expect some viscosity controlled capillary-induced blunting of the sharp features shown in these theoretical cross sections.

The existence of sharp cross-sectional features after the ion sculpting of nanopores is critical to obtaining high spatial resolution in ion beam sculpted single molecule detectors.[1] The inclusion of sputtering and surface tension effects into a morphology evolution model thus remains important work to be done to fully elucidate the practical implications of the predictions presented here. Further progress in high-resolution imaging of the cross-sectional geometry of ion sculpted nanopores would be another very important achievement.

## VI. SUMMARY

(1) Amorphous silicon nanopores close at 80 °C under continuous 3 keV $Ar^+$ ion irradiation of 0.24 $\mathrm{nm^{-2}\ s^{-1}}$.
(2) A "memory effect" is observed: at the same instantaneous radius, pores that started larger close more slowly.
(3) An ion-stimulated viscous flow model using the 3D constitutive relation of Otani *et al.* is developed. Four dimensionless parameters govern the model solutions: $fAt$, $h/R_0$, $fA\eta/E$, and $\nu$. Under the conditions of the experiment, the latter two parameters are insignificant for determining the morphology evolution. The sole remaining adjustable parameter is $A$, which can, in principle, be measured in independent experiments. Neglecting the effect of sputter erosion, $A$ takes the value $5 \times 10^{-17}$ $\mathrm{cm^2/ion}$ for these conditions. This is of the same order of magnitude as values found for mega-electron-volt ion irradiation of amorphous Si and $SiO_2$. The only existing mechanistic model for the origin of anisotropic deformation characterized by the parameter $A$ is a model based on electronic stopping, yet electronic stopping is only ~10% of the total stopping under our conditions and is very much less than the electronic stopping for the mega-electron-volt irradiation conditions for which the model was developed. Hence it is quite possible that another mechanism, such as isotropic dilatation from implantation plus sputter erosion from the topmost surface, is responsible for the anisotropic deformation effect under the conditions studied here.
(4) A simple analytical version of the model provides insight from dimensional analysis and predicts a closing rate given by Eq. (12).
(5) A finite-element solution of the full model exhibits surprising changes in cross-section morphology, which are untested experimentally.
(6) The finite-element solution reproduces the shape of the radius versus fluence curves and the sign and magnitude of the memory effect.
(7) To the extent permitted by the limited experimental resolution, the micrograph in Fig. 1 qualitatively confirms several cross-sectional geometry predictions of the finite-element viscous flow model.
(8) The viscous layer model does not reproduce several aspects of the experimental data that are reproduced by the adatom diffusion model—the effects of varying steady-state flux and of flux pulsing, and the effect of temperature.
(9) The two models and experiments on various materials are compared.

## ACKNOWLEDGMENTS

We thank Xi Wang and Joost Vlassak for *a*-Si sputter deposition. We thank Howard Stone for helpful discussions. Research supported by the U.S. Department of Energy, Office of Basic Energy Sciences, Division of Materials Sciences and Engineering under Award No. DE-FG02-06 ER46335. Research by J.A.G. was supported by the National Institutes of Health, Award No. 2R01HG003703. Research by J.W.H. was supported by the Harvard MRSEC under NSF (Grant No. DMR-0820484).

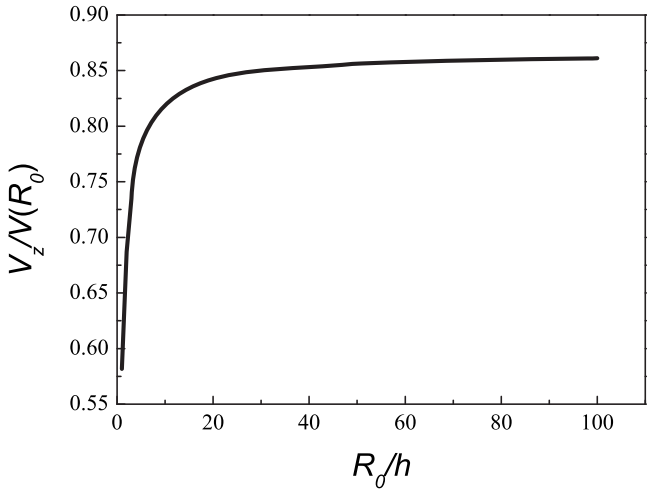


FIG. 7. Initial slope of trajectory of pore edge $A_1$, $v_Z/V(R_0)$, vs normalized pore radius $R_0/h$ in simple analytical model.

## APPENDIX

According to the small-deformation analytical model in Sec. III B, the instantaneous inward radial velocity $V(R)$ of the corner (Fig. 3) of a pore with instantaneous radius $R$, is given by Eq. (10). This model is strictly valid at the beginning of deformation when there is no overhanging unsupported film, but remains approximately valid during finite deformation under the assumption that the interaction with the unsupported portion of the film may be neglected. Assuming constant density during deformation, the initial axial velocity $v_Z$ of tip $A_1$ (Fig. 5) along the axial $z$ direction can be estimated as

$$-\frac{v_Z}{h}=\dot{\varepsilon}_{zz}|_{R_0}=-(\dot{\varepsilon}_{rr}+\dot{\varepsilon}_{\theta\theta})|_{R_0}, \tag{A1}$$

where $v_Z$ is reckoned as positive for motion in the direction of the ion beam (i.e., downward in Figs. 3 and 5) and the relevant strain rates are

$$\dot{\varepsilon}_{rr}=d\bar{v}/dr=\frac{-fA\left[-\frac{3}{2}K_0\left(\frac{\sqrt{3}r}{2h}\right)-\frac{\sqrt{3}h}{r}K_1\left(\frac{\sqrt{3}r}{2h}\right)\right]}{K_0\left(\frac{\sqrt{3}R}{2h}\right)+\frac{h}{\sqrt{3}R}K_1\left(\frac{\sqrt{3}R}{2h}\right)} \tag{A2}$$

and

$$\dot{\varepsilon}_{\theta\theta}=\bar{v}/r=\frac{-fA\left[\frac{\sqrt{3}h}{r}K_1\left(\frac{\sqrt{3}r}{2h}\right)\right]}{K_0\left(\frac{\sqrt{3}R}{2h}\right)+\frac{h}{\sqrt{3}R}K_1\left(\frac{\sqrt{3}R}{2h}\right)}. \tag{A3}$$

By substituting Eqs. (A2) and (A3) into Eq. (A1) we find

$$v_Z=\frac{\frac{3}{2}fAhK_0\left(\frac{\sqrt{3}R}{2h}\right)}{K_0\left(\frac{\sqrt{3}R}{2h}\right)+\frac{h}{\sqrt{3}R}K_1\left(\frac{\sqrt{3}R}{2h}\right)} \tag{A4}$$

and, further,

$$\frac{v_Z}{V(R)}=\frac{\sqrt{3}K_0\left(\frac{\sqrt{3}R}{2h}\right)}{2K_1\left(\frac{\sqrt{3}R}{2h}\right)}. \tag{A5}$$

The behavior of $v_Z/V(R)$ versus $R/h$ is shown in Fig. 7. Applied to the initial trajectories of two pores of differing initial radii $R_0$, it implies that the ratio $v_Z/V(R_0)$, i.e., the initial slope of the trajectory of the corner, is larger in magnitude if the initial pore size is larger. Thus, for the Si substrate with the larger value of $R_0$, the tip $A_1$ identified in Fig. 5 initially deflects downward more rapidly.

[1] J. Li, D. Stein, C. McMullan, D. Branton, M. J. Aziz, and J. Golovchenko, Nature (London) **412**, 166 (2001).
[2] J. Li, M. Gershow, D. Stein, E. Brandin, and J. A. Golovchenko, Nature Mater. **2**, 611 (2003).
[3] D. Fologea, M. Gershow, B. Ledden, D. S. McNabb, J. A. Golovchenko, and J. L. Li, Nano Lett. **5**, 1905 (2005).
[4] D. M. Stein, C. J. McMullan, J. L. Li, and J. A. Golovchenko, Rev. Sci. Instrum. **75**, 900 (2004).
[5] Q. Cai, B. Ledden, E. Krueger, J. A. Golovchenko, and J. L. Li, J. Appl. Phys. **100**, 024914 (2006).
[6] D. Stein, J. Li, and J. A. Golovchenko, Phys. Rev. Lett. **89**, 276106 (2002).
[7] E. Snoeks, A. Polman, and C. A. Volkert, Appl. Phys. Lett. **65**, 2487 (1994).
[8] E. Snoeks, T. Weber, A. Cacciato, and A. Polman, J. Appl. Phys. **78**, 4723 (1995).
[9] M. L. Brongersma, E. Snoeks, T. van Dillen, and A. Polman, J. Appl. Phys. **88**, 59 (2000).
[10] T. van Dillen, A. Polman, C. M. van Kats, and A. van Blaaderen, Appl. Phys. Lett. **83**, 4315 (2003).
[11] K. Otani, X. Chen, J. W. Hutchinson, J. F. Chervinsky, and M. J. Aziz, J. Appl. Phys. **100**, 023535 (2006).
[12] T. van Dillen, A. Polman, P. R. Onck, and E. van der Giessen, Phys. Rev. B **71**, 024103 (2005).
[13] L. E. Malvern, *Introduction to the Mechanics of a Continuous Medium* (Prentice-Hall, Upper Saddle River, New Jersey, 1969).
[14] Y.-R. Kim, P. Chen, M. J. Aziz, D. Branton, and J. J. Vlassak, J. Appl. Phys. **100**, 104322 (2006).
[15] ABAQUS, *ABAQUS 6.4 Theory Manual* (ABAQUS, Pawtucket, RI, 2004).
[16] I. Yamamoto, N. Kasai, and S. Nishimoto, Jpn. J. Appl. Phys., Part 1 **37**, 1256 (1998).
[17] J. F. Ziegler, J. P. Biersack, and U. Littmark, *The Stopping and Range of Ions in Matter* (Pergamon, New York, 1985).
[18] S. Vauth and S. G. Mayr, Phys. Rev. B **75**, 224107 (2007).
[19] R. S. Averback and T. Diaz de la Rubia, in *Solid State Physics: Advances in Research and Applications*, edited by H. Ehrenreich and F. Spaepen (Academic, New York, 1998), Vol. 51, p. 281.
[20] H. Gnaser, *Low-Energy Ion Irradiation of Solid Surfaces (Springer Tracts in Modern Physics)* (Springer, Berlin, 1999), Vol. 146.
[21] G. Wallner, M. S. Anand, L. R. Greenwood, M. A. Kirk, W. Mansel, and W. Waschkowski, J. Nucl. Mater. **152**, 146 (1988).
[22] T. Mitsui, D. M. Stein, Y.-R. Kim, D. Hoogerheide, and J. A. Golovchenko, Phys. Rev. Lett. **96**, 036102 (2006).
[23] H. B. George, *Ion-Stimulated Mass Transport in Nanoscale Morphology Evolution* (Harvard University Press, Cambridge, 2007).
[24] T. van Dillen, M. J. A. de Dood, J. J. Penninkhof, A. Polman, S. Roorda, and A. M. Vredenberg, Appl. Phys. Lett. **84**, 3591 (2004).
[25] H. H. Chen, O. A. Urquidez, S. Ichim, L. H. Rodriguez, M. P. Brenner, and M. J. Aziz, Science **310**, 294 (2005).
[26] H. P. Bonzel and M. Nowicki, Phys. Rev. B **70**, 245430 (2004).